Additive manufacturing enabled synergetic strengthening of bimodal reinforcing particles for aluminum matrix composites

Siming Ma[1], Zhongxia Shang[2], Anyu Shang[2], Peter Zhang[1], Chenglu Tang[1], Yuze Huang[3,4], Chu Lun Alex Leung[3,4], Peter D. Lee[3,4], Xinghang Zhang[2], Xiaoming Wang[1*]

[1]School of Engineering Technology, Purdue University, West Lafayette, IN 47907 USA

[2]School of Materials Engineering, Purdue University, West Lafayette, IN 47907, USA

[3]UCL Mechanical Engineering, University College London, WC1E 7JE, London, UK

[4]Research Complex at Harwell, Harwell Campus, Didcot, OX11 0FA, UK

*Corresponding Email: wang1747@purdue.edu

Abstract

An additive manufactured TiB_2/Al-Cu-Mg-Ni composite with a minor amount of Sc was fabricated by laser powder bed fusion (LPBF). The composite shows a yield strength of ~370 MPa, almost doubling the strength of its wrought matrix counterpart, and an elongation of ~7 %. The superior mechanical properties are attributed to a unique micro-nano hierarchical microstructure, consisting of nanoscale and microscale TiB_2 particles dispersed in a matrix of fine aluminum grains (3 μm) together with intragranular intermetallic nanoparticles and nano-cellular networks (cell size 30 nm). The formation of the TiB_2 nanoparticles is the consequence of partial dissolution of the TiB_2 particulates and the enrichment of Sc in the newly formed nanoparticles.

Remarkable strengthening effects are achieved by the bimodal TiB_2 particles, intermetallic nanoparticles and intragranular nano-cellular networks. This study provides new insights into the role of additive manufacturing in tailoring the microstructure of particulate reinforced metal matrix composites (MMCs) with advanced properties.

Keywords: Additive manufacturing, Metal matrix composite, TiB_2/Al, Al-Sc, Al2618

1. Introduction

Additive manufacturing (AM) of aluminum alloys shows a great potential for the rapid fabrication of complex geometric components in the aerospace and automotive industries [1–3]. Among different AM technologies, laser powder bed fusion (LPBF) is broadly chosen in processing aluminum alloys and aluminum matrix composites [4,5]. Al-Si casting alloys, such as AlSi10Mg [6], are common alloys for LPBF attributed to their excellent printability. But their applications are limited by medium strength and low ductility. Meanwhile, wrought aluminum alloys, such as Al–Cu–Mg (2xxx series), have superior strength and ductility, but suffering from a high susceptibility to cracking during LPBF. The mechanical properties of AM Al–Cu–Mg alloys are, therefore, not comparable with their wrought counterparts [7]. AM of high strength Al–Cu–Mg alloys remains challenging.

Efforts have been made by adding a high concentration of Sc and Zr as inoculants

in various aluminum alloys to enhance the printability and mechanical properties by forming Al_3(Sc, Zr) intermetallic particles, such as Scalmalloy®, designed for AM lightweight and high-performance components of complex geometry for the aerospace industries [8–12]. However, despite of the superior mechanical properties, such strategy is hindered economically by a high percentage of Sc addition. An alternative method is to fabricate particulate reinforced metal matrix composites (PRMMCs) [5]. Particle reinforcements not only strengthen the aluminum matrix but also act as heterogeneous nuclei promoting fine equiaxed aluminum grains and, therefore, reducing the susceptibility to cracking [13]. Moreover, extraordinary strengthening is enabled by LPBF of PRAMCs compared to tradition casting methods. First, the extremely high cooling rate (~10^5–10^6 K/s) of LPBF activates a large fraction of the reinforcing particles as effective nuclei for grain refinement [14,15], causing an improved grain boundary strengthening effect. Additionally, the Marangoni melt flow during LPBF benefits a uniform dispersion of the reinforcing particles, enhancing particle strengthening effects by alleviating possible particle clustering [16]. Furthermore, the high temperature of the melt pool potentially causes the decomposition or dissolution of the reinforcing particles and their reprecipitation subsequently [17,18], resulting in the refinement of reinforcing particles for an enhanced strengthening effect.

Amongst the reinforcements, TiB_2 particulates are particularly favorable as both a good grain refiner and a reinforcing phase for aluminum alloys [19,20], and can be fabricated in-situ in Al alloys and subsequently gas-atomized to TiB_2/Al composite feedstock powders for AM [21–23]. LPBF aluminum alloys with in-situ TiB_2

particulates outperform their composites with ex-situ particulates, in terms of finer particle size and superior mechanical properties [23–25]. Moreover, further modification with a small amount of rare-earth elements, such as Sc, promotes the refinement and dispersion of TiB_2 reinforcing particulates [26,27], benefiting a better mechanical performance. Additionally, although it is still questionable whether TiB_2 particles survive melting or dissolve and reform upon the rapid cooling under the high temperature in the melt pool, such process is suggested in recent studies [18,28,29]. TiB_2 particles can be partly melted and reprecipitate as ultrafine nanoparticles during LPBF, showing remarkable strengthening effect [18].

AM also refines intermetallic phases remarkably to metastable nano-sized particles or precipitates, resulting in a considerable strengthening effect due to their ultrafine size, for example, nano-Si precipitates in AlSi10Mg alloys [23]. In LPBF Al-Cu-Mg alloys modified by TiB_2 particulates, Cu/Mg-rich compounds are distributed mostly in intergranular zones, while nano-sized precipitates are scarcely seen inside the aluminum grains [22,30]. In comparison, a recent work reported that a high number density of nano-sized Al_3Ni intermetallic particles dispersed ubiquitously in a LPBF Al-Ni alloy, causing an evident strengthening effect [31]. The formation of ultrafine Al_3Ni intermetallic particles is attributed to the lower diffusivity and solubility of Ni in Al, compared to Cu and Mg [32,33]. Moreover, nano-sized Al-Cu-Ni type intermetallics are also revealed in several LPBF aluminum alloys [34,35], which have higher hardness and moduli than Al_3Ni, promising to provide an enhanced strengthening effect [36,37]. The addition of Ni in Al-Cu-Mg alloy is, therefore,

inspired for LPBF to obtain a large density of fine-sized Al-Cu-Ni type intermetallic particles with a considerable strengthening potential. Furthermore, Al-Cu-Ni type intermetallics have good thermal-stability [31,37], enabling potential applications at elevated temperatures [38].

The paper reports our findings on a LPBF Al-Cu-Mg-Ni composite that is reinforced with in-situ TiB_2 particulates and modified with small amount of Sc. The as-built composite delivers outstanding mechanical properties, attributed to its unique refined micro-nano architectured microstructure enabled by AM. The microstructure is characterized by fine aluminum grains with uniformly dispersed TiB_2 particulates in the micrometer level, while a high number density of intermetallic and TiB_2 particles disperse ubiquitously throughout of the aluminum grains at a nanoscale. The presence of an ultrafine cellular structure that is defined by three-dimensional networks is also revealed within each aluminum grain. The behavior of reinforcing particles during LPBF and their effects on strengthening are revealed, shedding light on the great potential of AM on the design of high strength aluminum matrix composites.

2. Material and methods

TiB_2 particulates were produced in-situ via chemical reactions of a mixture of KBF_4 and K_2TiF_6 salts with the molten Al matrix in an induction furnace at 730 °C for 30 min [39]. The TiB_2/Al composite melt was stirred by an electromagnetic force in an induction furnace and the slag was removed before casting into ingots. The ingots were

remelted and gas-atomized into feedstock powders that are dispersed with the in-situ TiB_2 particulates. Powders that are falling in the range of 15~65 μm in size were chosen for LPBF (Fig. 2(a)). Both one-inch cubes and dog-bone shaped tensile specimens were printed using a Renishaw RenAM400^{TM} additive manufacturing machine with a spot size of 70 μm. The specimens were built layer-by-layer with a rotation of 90° in orientation between two consecutive layers on an aluminum alloy baseplate without preheating. The hatching distance and layer thickness were set as 100 μm and 25 μm, respectively. A high purity argon gas atmosphere was maintained to minimize oxidation during processing. The laser power and scan speed were optimized as 90 W and 1200 mm/s, respectively, after evaluating the density of the one-inch cubes and the mechanical properties of the as-printed samples with different processing parameters (Fig. S2). The chemical compositions of the feedstock powder and the LPBF composite are given in Table S1, referring to the composition of commercial Al2618 alloy with a low Fe content and the addition of 0.11 % Sc. The volume fraction of TiB_2 particulates is 4.9 %.

Dog-bone shaped samples with the gauge length of 25.4 mm, width of 6 mm, and thickness of 3 mm were uniaxial tensile tested following the ASTM E8 standard. The tests were conducted on an ATS900 machine at room temperature (25 °C) at a strain rate of 10^{-3} s^{-1}. The tensile direction was perpendicular to the build direction (BD). Three parallel tensile tests were conducted. For comparison, samples of the TiB_2/Al composite and matrix alloy ingots were subjected to traditional hot rolling, which were described in a previous work [40] and in Supplementary Material A. Micro-CT 3D

scanning was conducted on a Zeiss Xradia 510 Versa^{TM} machine, to examine the distribution of TiB_2 particulates and pores inside the bulk sample at a resolution of 5.8 micrometers and a zoom-in resolution of 1 μm. Polished specimens were etched by using a Keller's reagent for microstructural analyses using a Leica DM-LM/P optical microscope (OM), followed by a detailed analysis with a Quanta 3D field emission scanning electron microscope (FESEM) in a backscattered electron (BSE) imaging mode, equipped with an energy dispersive X-ray spectrometer (EDS) under 10 kV accelerating voltage. Electron backscattered diffraction (EBSD) experiments were operated at an acceleration voltage of 15 kV and a working distance of ~ 15 mm with a scanning step size of 0.1 μm on an FEI Quanta 650 with a field emission gun (FEG), and a MAIA3 TESCAN field emission scanning electron microscope (SEM) with a scanning step size of 0.34 μm. The acquired data were processed using the orientation imaging microscopy (OIM) software. The data with a confidence index (CI) value greater than 0.1 were used to ensure the quality and reliability of the orientation maps. Samples for transmission electron microscopy (TEM) were prepared by mechanical grinding and punching into 3 mm disks followed by electro-polishing with a nitric acid-methanol solution (1:3 in volume ratio) at -20°C under a voltage of 15 V. TEM analyses and corresponding EDS chemical mapping were carried out on a Thermo-Fischer FEI Talos 200X TEM microscope operated at 200 kV equipped with a high angle annular dark field (HAADF) detector and SuperX EDS with four silicon drift detectors. All the EDS maps were captured under the drift correction mode. Image analyses were conducted by the ImageJ software for the measurement of grain size, as well as the size

and volume fraction of TiB_2 and intermetallic phases. Fast Fourier Transform (FFT) of the HRTEM images was conducted by using DigitalMicrograph^{TM} software. Electron diffraction patterns were simulated with CryTBox software for indexing the phases [41].

Furthermore, to help understand the microstructure evolution in the melt pool during LPBF, a 3D heat-transfer FE simulation was performed to simulate a single-track laser beam scanning across the sample with a moving Gaussian heat source via the commercial software Abaqus. The simulation is described in detail in Supplementary Material B. Additionally, in order to measure the solidification front velocity (SFV) in LPBF, the melt pool of a 7-series commercial aluminum alloy was in-situ monitored using a high-speed synchrotron X-ray imaging technique with an identical scanning velocity to the studied LPBF TiB_2/Al composite for reference. The details of the technique were given in a previous paper [42].

3. Results

The tensile stress-strain curves of the LPBF TiB_2/Al composite against its hot-rolled counterparts are shown in Fig. 1(a). The as-build composite exhibits a yield strength (YS) of 367.4 ± 2.7 MPa, ultimate tensile strength (UTS) of 451.5 ± 2.8 MPa and elongation of 6.5 ± 0.4 %. A yield plateau is clearly seen from the stress-strain curve of the as-built composite, ranging from the yield point to a nominal strain of approximately 0.02 due to the propagation of the Lüders bands, similar to the findings in other LPBF TiB_2/Al-Cu alloys [22,30]. The LPBF composite has a remarkable

improvement both in strength and ductility, compared to its hot-rolled matrix alloy and composite counterparts at both as-rolled and T6 states. The UTS of the LPBF composite is nearly doubled compared to that of the as-rolled matrix alloy and composite, and also superior to those of T6 treated. From Fig. 1(b), the as-built TiB_2/Al composite in this study exhibits a superior UTS than other reported as-built LPBF Al-Cu-Mg alloys (such as Al2024, A205 and Al2618 alloys) [24,43–45] and their composites reinforced by TiB_2 particulates [22,24,30,43,46–49]. Furthermore, without heat treatment, the as-built TiB_2/Al composite exhibits a higher UTS and a comparable elongation to failure, compared to the majority of T6 treated commercial wrought Al2618 alloys [37,38,45,50–55]. Meanwhile, the as-built composite with only 4.9 vol. % in-situ TiB_2 particulates reaches a comparable UTS and an improved elongation than the T6 treated wrought Al2618 matrix composites reinforced with a 10~20 % volume/weight fraction of ex-situ Al_2O_3 or SiC particles in other studies [50,52].

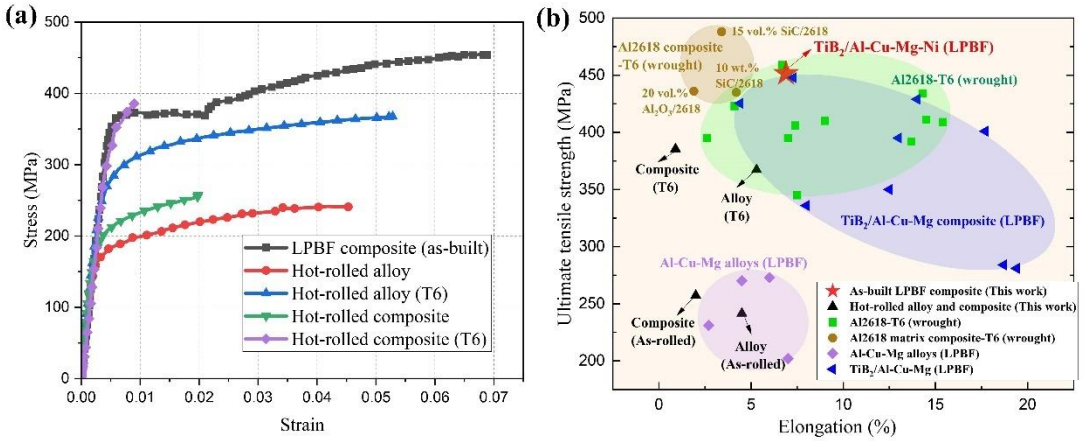

Fig. 1. (a) Representative engineering stress-strain curves of the LPBF TiB_2/Al composite in comparison to the hot-rolled alloy and composite counterparts. (b) The comparison of mechanical properties of LPBF and T6-state wrought Al-Cu-Mg alloys and composites in literatures [20,22,28,35,36,40–53].

An overview of the microstructure of the LPBF composite is given in Fig. 2. Fig. 2(a) presents the feedstock powders with a high degree of sphericity. TiB_2 particulates are dispersed throughout of the powders, both on the surfaces and inside the powders, as shown in Fig. 2(a), inserted a size distribution of the powders. A reconstructed 3D OM image in Fig. 2(b) shows fish-scale patterns along BD, formed by the layer-by-layer solidified melt pools. A 3D reconstructed BSE image of the composite is presented in Fig. 2(c). The bright particulates refer to TiB_2, which are dispersed uniformly in all three directions. Micro-CT 3D scanning in Fig. 2(d) shows the spatial distribution of pores and TiB_2 particulates throughout a cylindrical sample without discernable cracks. The smaller purple particles refer to individual TiB_2 particulates, while the blue, green and red-colored ones are micro-pores. Most pores are spherical while a few of them are elongated perpendicular to BD. The pores have a maximum equivalent diameter of 70 μm with a majority being smaller than 50 μm, as shown in Fig. 2(e). The total porosity of the LPBF composite is approximately 1.5 % in the observed region. The EBSD mappings in Figs. 2(f) and (g) reveal a fine equiaxed grain structure with an average grain size of 3.1 ± 0.4 μm of the LPBF composite. No obvious texture can be identified from the random coloration of the EBSD IPF image. The unindexed black zones, as noted in Figs. 2(f) and (g), refer to TiB_2 particulates or their clusters, which are distributed mainly at grain boundaries with sizes of the micrometer level. Compared to its hot-rolled composite counterpart in Fig. S1(d), the dispersion of the micro-sized TiB_2 particulates in the LPBF composite is homogenized and the grain size is reduced

remarkably from ~50 μm to ~3 μm.

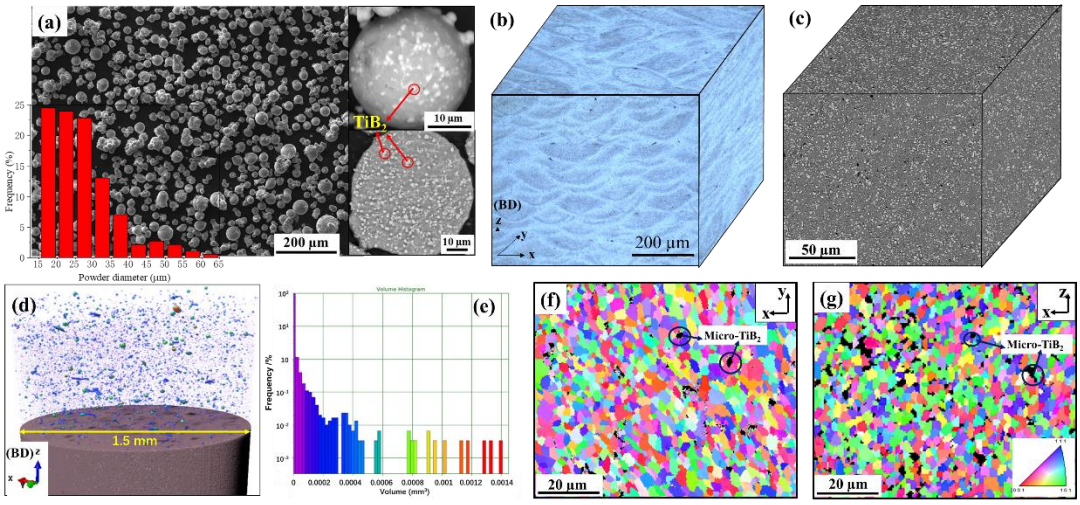

Fig. 2. (a) SEM images showing the morphology and the cross-section microstructure of TiB_2/Al composite powders, inserted a size distribution of the powders. Constructed 3D (b) OM and (c) backscattered electron (BSE) images of the LPBF composite. (d) A micro-CT image shows the spatial distribution of pores and TiB_2 particulates with (e) the size distribution histogram. (f, g) EBSD inverse pole figures (IPF) map of the LPBF composite taken from x-y and x-z plane, respectively (Z axis refers to BD).

Fig. 3(a) presents a local SEM BSE image across a melt pool boundary, showing a refined microstructure of the LPBF composite with uniformly dispersed micro-sized TiB_2 particulates against the background filled with nano-sized intermetallics, compared to the severely agglomerated TiB_2 particulates and coarse intermetallics in its hot-rolled counterpart (Fig. S1). The size and distribution of TiB_2 particulates show no evident differences with respect to the melt pool boundary. The coarsening of the intermetallics near the melt pool boundary, as reported in other studies [22,56], is not seen clearly in the TiB_2/Al composite. The HAADF-STEM image in Fig. 3(b) gives a

magnified view of the refined intermetallics in multiple aluminum grains. The intermetallics appear either as elongated rods along the grain boundaries or as discrete spherical nanoparticles with a fairly high number density throughout the aluminum grains. EDS elemental mappings in Fig. 3(c1) and (c2) show the intermetallics being enriched in either Cu or Ni or both, while Mg is only partly enriched in the intermetallics and tends to be a solute element in the aluminum matrix as seen from Fig. 3(c3). Moreover, from the elemental mapping of Ti in Fig. 3(c4), it is interesting to note that plenty of Ti-enriched tiny spots are seen ubiquitously throughout the aluminum grains, which are likely fine-sized TiB_2 particles that are not directly seen in the SEM images in Fig. 3(a). The findings suggest the existence of intragranular TiB_2 nanoparticles in the LPBF composite, which will be further analyzed later. Additionally, high density dislocations are observed inside the grains, associated with the intragranular nanoparticles as shown in the TEM-BF image of Fig. 3(d). Fig. 3(e) presents the HAADF image of several micro-sized TiB_2 particulates (noted as micro-TiB_2 thereafter) with corresponding elemental mappings of Ti, B and Sc. Evidently, Sc is enriched in these diboride particulates. The enrichment suggests the formation of $(Ti,Sc)B_2$ solid solution compounds through substitution of Ti by Sc [57]. A near-rational orientation relationship (OR) between a micro-TiB_2 particle and the aluminum matrix is elucidated from the FFT patterns from the HRTEM images in Fig. 3(f). The OR is elucidated as TiB_2 $[11\bar{2}0]$ // Al [110] and TiB_2 (0001) // Al $(\bar{1}11)$, indicating a highly coherent interface as commonly reported in studies on nucleation of α-Al on TiB_2 particulate [58,59]. The size distributions of the TiB_2 and intermetallic particles

are presented in Figs. 3(g) and (h), respectively, by quantitative analyses from a series of SEM and TEM images. The micro-TiB_2 particulates in the LPBF composite (Fig. 3(a)) follow a typical lognormal size distribution, averaging at 0.784 μm. From Fig. 3(g), the average size of the micro-TiB_2 particulates in the LPBF composite is slightly increased than that in its hot-rolled counterpart (Fig. S1(d)). The intragranular intermetallics and TiB_2 nanoparticles (noted as nano-TiB_2 thereafter) are ultrafine in sizes, averaging at ~70 nm and ~30 nm, respectively, as presented in Fig. 3(h).

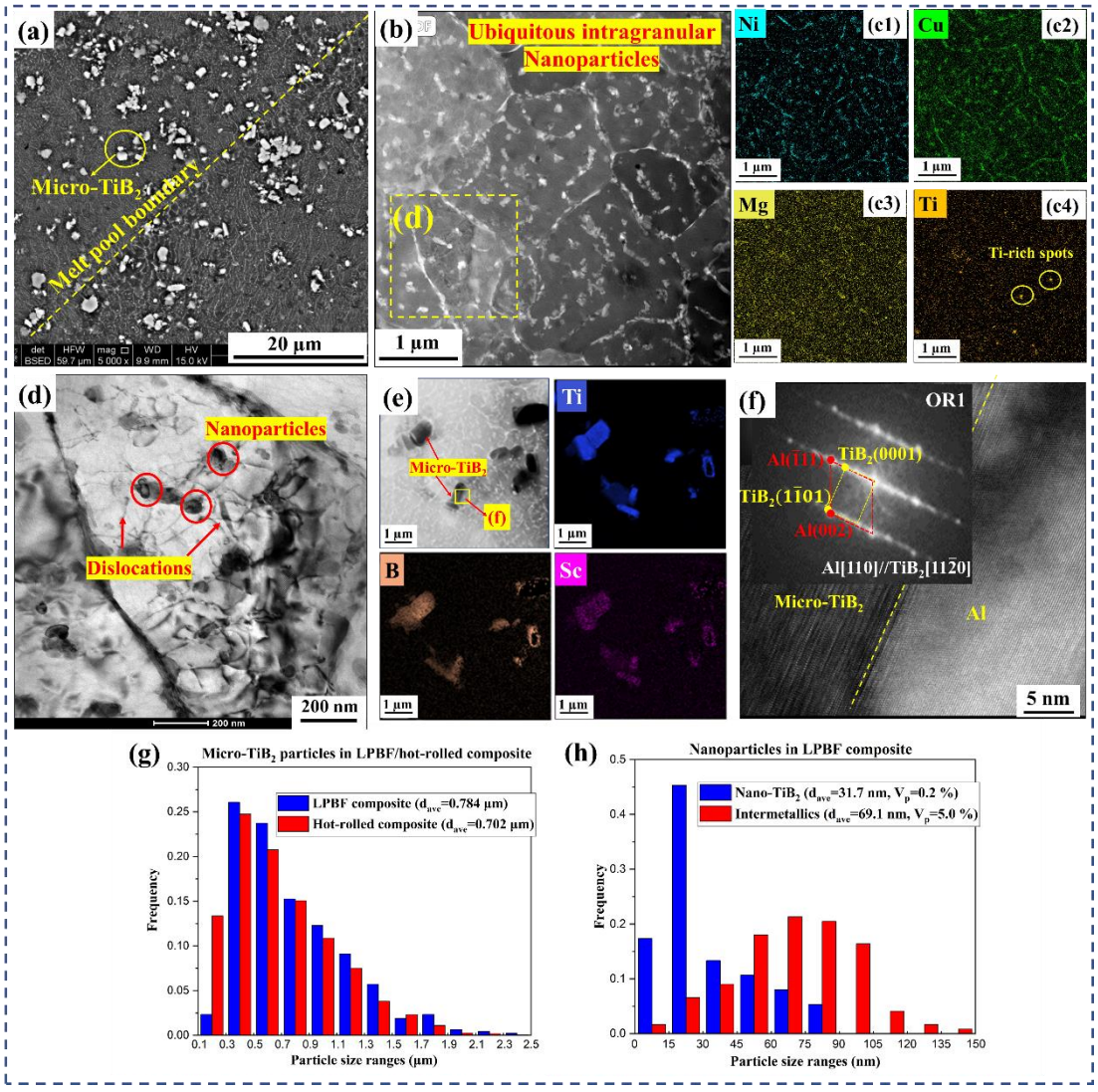

Fig. 3 (a) A high magnification BSE image of the LPBF composite showing micro-TiB_2

particulates with refined intermetallics presented in the background; (b) HAADF STEM image showing ubiquitous distributed nanoparticles in several aluminum grains with (c1~c4) corresponding EDS elemental maps; (d) Local magnified TEM bright field (BF) image showing high density dislocations associated with intragranular nanoparticles; (e) HAADF image of several micro-TiB_2 particulates with corresponding elemental mapping of Ti, B and Sc; (f) HRTEM image of a coherent micro-TiB_2/Al interface with corresponding FFT patterns; Size distributions of (g) the micro-TiB_2 particulates in the LPBF and hot-rolled composites, and (h) nano-TiB_2 and intermetallic nanoparticles in the LPBF composite.

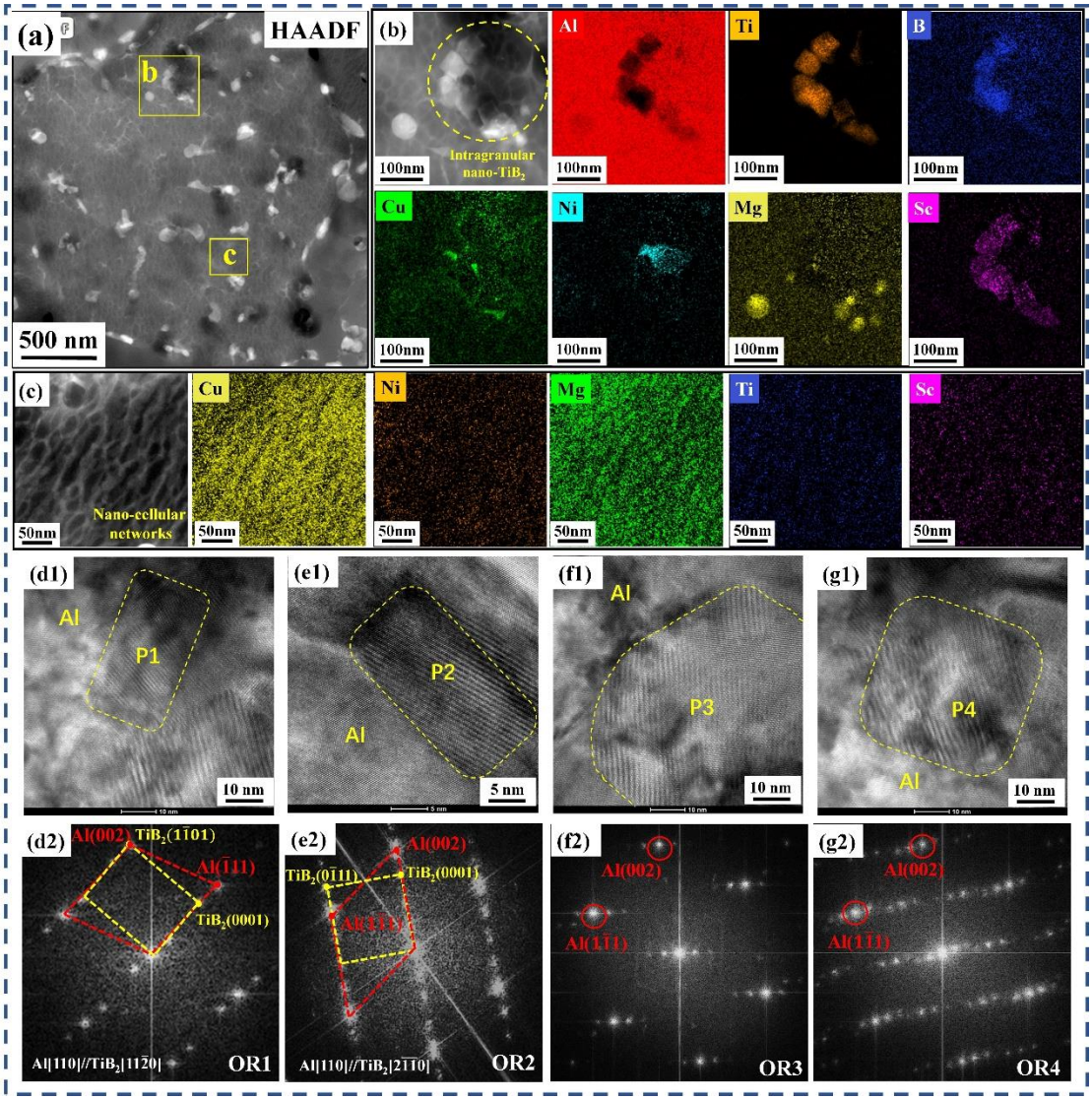

Fig. 4 (a) HAADF image showing the intermetallic nanoparticles and nano-TiB_2 in an

aluminum grain; (b) Local magnified box b in Fig. 4(a) showing nano-TiB_2 particles engulfed in aluminum matrix with corresponding EDS elemental maps; (c) Local magnified box c in Fig. (a) showing the nano-cellular networks with corresponding EDS elemental maps; (d1~g1) HRTEM images taken from Al [110] axis showing four individual nano-TiB_2 particles inside the grains with the corresponding FFT patterns of the nano-TiB_2/Al interface shown in (d2~g2), respectively.

The HAADF image in Fig. 4(a) furtherly reveals the microstructural details inside an aluminum grain, showing uniformly dispersed intragranular nanoparticles against the background filled with ultrafine nano-cellular networks. Fig. 4(b) presents several nano-TiB_2 particles in the aluminum grain with corresponding EDS elemental maps. It is found that Sc is also enriched in the nano-TiB_2 particles, the same as the case of micro-TiB_2 particulates in Fig. 3(e). The magnified HAADF image in Fig. 4(c) shows an ultrafine nano-cellular network structure. The cell width is approximately 30 nm in average. The cell walls are less than 10 nm in diameter enriched in Cu and Mg as shown from its corresponding EDS maps. The interfaces between several intragranular nano-TiB_2 and aluminum matrix reveal potential ORs from a number of HRTEM images in Figs. 4(d1~g1). Different ORs are suggested from their corresponding FFT patterns in Figs. 4(d2~g2). Fig. 4(d2) suggests the same OR (OR1) between particle P1 and aluminum matrix as the OR between micro-TiB_2/Al in Fig. 3(f). Meanwhile, another OR (OR2) between the nano-TiB_2 particle (P2) and aluminum matrix is suggested as TiB_2 $[2\bar{1}\bar{1}0]$ // Al [110] and TiB_2 (0001) // Al (001), as shown in Fig. 4(e2). Both OR1 and OR2 are well documented low-energy crystallographic relationships between TiB_2 and α-Al [59]. Moreover, other ORs deviated from the above two systematic

crystallographic orientation relationships (OR1 and OR2) are also revealed between P3, P4 and aluminum matrix as Figs. 4(f2) and (g2), noted as OR3 and OR4, respectively. The presence of these ORs suggests that the engulfed nano-TiB_2 particles can either perform a systematic or a random OR with α-Al.

4. Discussion

The LPBF TiB_2/Al composite exhibits a unique refined micro-nano hierarchical microstructure. Aluminum matrix of equiaxed aluminum grains of ~3 μm in size is reinforced by uniformly dispersed bimodal TiB_2 ceramic particles (micro-TiB_2 of ~0.8 μm and nano-TiB_2 of less than 100 nm in sizes). The intermetallics are also greatly refined to a high number density of nanoparticles together with nano-cellular networks consisting of Cu/Mg-rich cell walls ubiquitous distributed inside aluminum grains. Attributing to the LPBF processing, the resultant microstructure of the TiB_2/Al composite is refined significantly comparing with the microstructure of the hot-rolled composites (Fig. S1). In the following paragraphs, the underlying mechanisms for the formation of such microstructure, as well as the correlation between the particular microstructural features and the outstanding mechanical properties will be discussed.

4.1.Microstructure evolution during LPBF

As shown in Fig. 2(d), elongated pores are typical observed in the LPBF composite. Such elongated pores are suggested to form at the melt pool boundaries due to the lack-

of-fusion during the layer-by-layer building process or the presence of oxidized powders, from in-situ synchrotron X-ray imaging of the LPBF process in related studies [42,60]. The lack-of-fusion elongated pores in the LPBF composite indicate non-fully melting in certain areas. The melting mode is therefore suggested as in the conduction regime, in which heat transfer dominates over convection. As a result, as applied in related studies [43,61], a 3D heat-transfer FE simulation was performed to describe the temperature distribution and relevant solidification parameters, such as cooling rate, thermal gradient, and SFV, in the melt pool upon a single laser beam scanning of the composite powders (see Supplementary Material B) without considering the hydrodynamics. The microstructural evolution of the TiB_2/Al composite during the rapid melting and solidification in the melt pool is illustrated as follows, referring to the FE simulation results in Fig. 5(a) and Fig. 6.

As the laser beam scans over a certain location, its temperature increases instantly to a maximum around 2300 °C in the melt pool, as shown in Fig. 6(a). The aluminum alloy is melted, leaving TiB_2 particulates in the liquid Al pool. Previous studies assumed, in general, that TiB_2 particulates are thermally stable and maintain their size and composition during LPBF since the maximum temperature in the melt pool is lower than the melting point of TiB_2 [23]. However, recent studies suggested that TiB_2 can be partially melted under high temperature in the melt pool [18,46]. The dissolution of TiB_2 in aluminum melt is as small as 10^{-11}, close to zero at 700 °C [20], but increases rapidly with the increase of temperature. At 1300 °C, the solubility reaches 0.035 wt.% Ti and 0.016 wt.% B, equivalent to 0.051 wt.% TiB_2 [62]. Thus, the dissolution of TiB_2

in aluminum is highly probable under the high temperature during LPBF, presented by the diffusion of Ti and B solute elements in the molten aluminum alloy [63], and rapidly dispersed by a turbulent flow of relatively high fluid velocity (> 0.5 m/s) [64,65]. Meanwhile, the Marangoni convection within the pool induces a capillary force promoting the uniform dispersion of the remaining micro-TiB_2 particulates [66,67], as shown schematically in Fig. 5(c1).

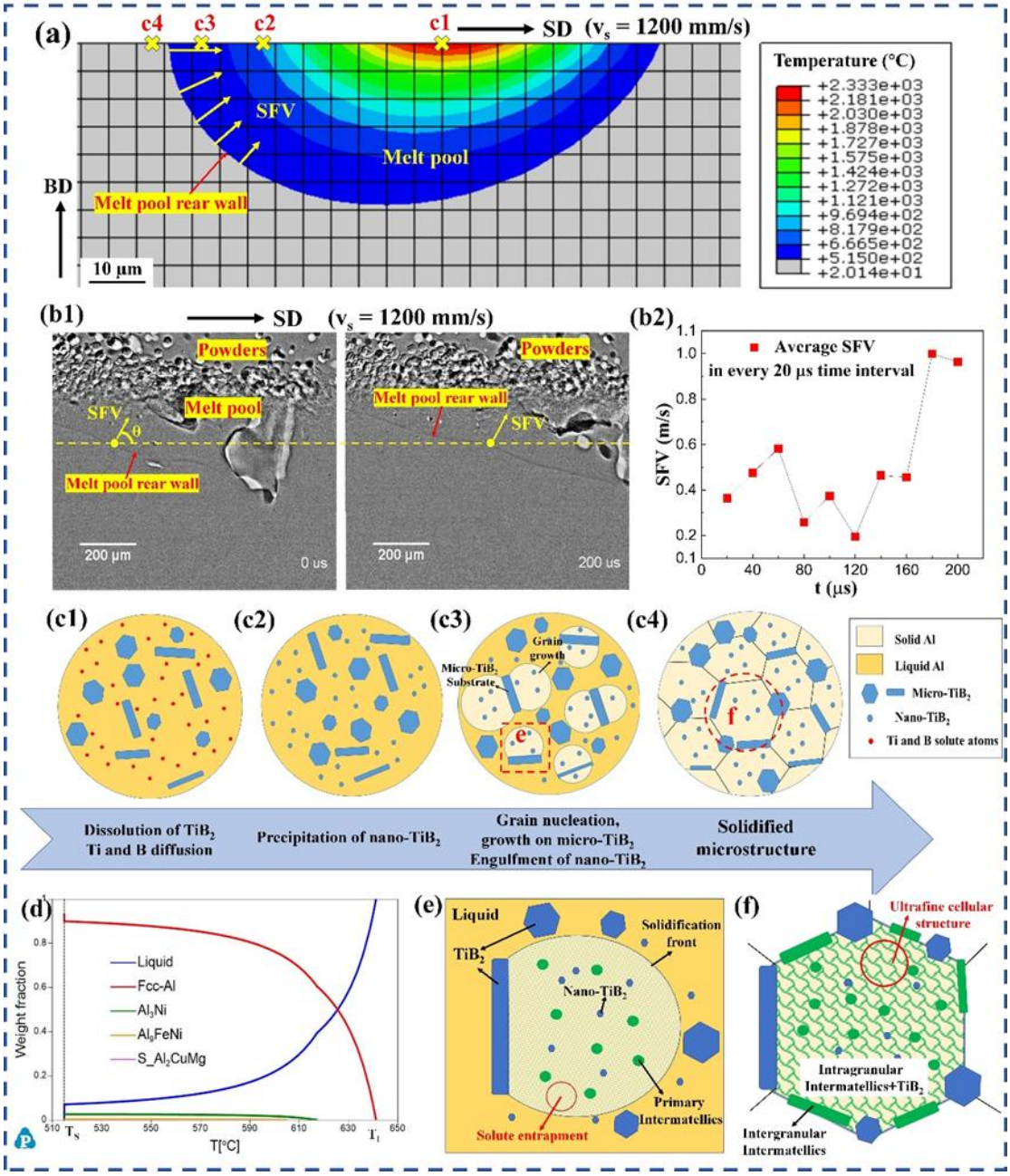

Fig. 5. (a) The simulated temperature field within the melt pool from the cross-section view during the single track LPBF process (Temperature of the gray colored region is lower than the solidus temperature of the aluminum matrix. SD refers to the scanning direction). (b1) Real-time observation of LPBF of aluminum alloy with the scanning velocity of 1200 mm/s identical to this study. (b2) The average SFV at the mid-depth of the melt pool in every 20 μs time interval measured from Fig. (b1). (c1~c4) Schematic images showing the typical microstructure evolution of the TiB_2/Al composite during the solidification of the melt pool. (d) Evolution of the phase fraction

in the matrix alloy simulated under the Scheil solidification condition. (e, f) Schematic images showing the evolution of intermetallics during the solidification of the melt pool.

As the laser beam moving forward, the melt pool cools down rapidly, resulting in the co-precipitation of Ti and B solute elements into ultrafine nano-TiB_2 particles (down to ~10 nm) ubiquitously dispersed in the aluminum melt, as shown schematically in Fig. 5(c2) and observed in Figs. 3 and 4, which have been rarely reported in various cast and AM TiB_2/Al composites [21–23,68]. Due to an extremely high cooling rate (at a magnitude of 10^6~10^7 K/s) and a short dwell time (less than 0.1 ms) as simulated in Fig. 6(c), the precipitated TiB_2 particles show an ultrafine size (~10 nm) under the large undercooling without enough time for coarsening, as proposed in a LPBF TiB_2/TiAl composite [18] and a rapidly solidified TiAl-B alloy [69]. Meanwhile, the enrichment of Sc in both micro-TiB_2 and nano-TiB_2 particles is revealed as shown in Figs. 3(e) and 4(b), respectively. The enrichment of Sc in TiB_2 was also observed by others when 0.1 wt. % Sc was introduced into CP-Al alloys that was grain refined by Al-5Ti-1B [57]. It was proposed that the diffusion of Sc into TiB_2 nanoparticles is appreciated by substituting Ti [70]. In this study, the addition of 0.11 wt. % Sc also results in the diffusion of Sc into micro-TiB_2 particulates. In addition, it is more likely that Sc and Ti co-precipitate with B to form (Ti,Sc)B_2 nanoparticles in the melt during LPBF [71]. The enrichment of Sc in the TiB_2 reduces the interfacial energy and increasing the interfacial wettability, which improves the dispersion and restricts the growth of nano-TiB_2 nanoparticles [27]. Additionally, the preferential adsorption of Sc on the $\{1\bar{2}12\}$, $\{11\bar{2}0\}$, and $\{10\bar{1}1\}$ planes of TiB_2 inhibits the growth of these facets effectively,

promoting the formation of polyhedral or quasispherical nano-TiB_2 particulates [26]. The precipitated TiB_2 nanoparticles in this study are generally equiaxed therefore, different from the plate-shaped TiB_2 nanoparticles observed in other studies without Sc addition [18,69].

Subsequently, solidification of the melt pool begins with the nucleation and growth of aluminum grains, when the melt pool continues to cool down to the solidification temperature range of the aluminum matrix. The rapid solidification of the studied aluminum alloy matrix is simulated under the Scheil condition as shown in Fig. 5(d), given the corresponding chemical composition of the aluminum matrix. The result shows that the solidification is initiated at 641 °C (T_l) and completed at 515 °C (T_s). According to the free growth model [72], the nucleation and free growth of a grain from an inoculate particle at an undercooling inversely proportional to the particle diameter. Due to the rapid cooling of AM and, therefore, a large degree of undercooling, the micro and even submicron-sized particulates are activated as nucleation substrates [14,15]. As a result, a high number density of micro-TiB_2 particulates is activated for the heterogeneous nucleation of aluminum grains, as illustrated in Fig. 5(c3), preferentially forming a coherent interface with aluminum matrix (OR1), as shown in Fig. 3(f). The grains are significantly refined, therefore. According to the interdependence model [73], the grain size (d_{gs}) is predicted as the sum of the distance of nucleation free zone (x_{NFZ}) and the distance to the next activated nucleant particle (x_{sd}) as Eq. 1.

$$d_{gs} = x_{NFZ} + x_{sd} \quad (1)$$

Under the rapid solidification condition associated with laser melting, x_{NFZ} can be significantly decreased to a magnitude of 10^{-2} μm [14], due to the high grain growth velocity and a less degree of dependency on the solute content of the alloy. As a result, x_{NFZ} is much smaller compared to the grain size and can be neglected. The grain size d_{gs} is approximately equal to x_{sd}. x_{sd} is related to the interparticle spacing of the activated micro-TiB_2 particulates of this study, which can be calculated as Eq. 2 [74].

$$x_{sd} = 1.12\frac{d_p}{(V_p^*)^{1/3}} \quad (2)$$

where d_p and V_p^* is the average size and the volume fraction of the activated TiB_2 particulates, respectively. In the studied LPBF TiB_2/Al composite, assuming a uniform dispersion of micro-TiB_2 particulates with an average size of d_p (0.784 μm) and taking x_{sd} as the grain size d_{gs} (3.1 μm), V_p^* is estimated as 2.3 % from Eq. 2, which is almost 50 % of total volume fraction of TiB_2 particles (V_p=4.9 %).

Additionally, from Fig. 3(c4) and Fig. 4(b), nano-TiB_2 particles are commonly located inside the aluminum grains, contradictory to other observations that TiB_2 nanoparticles are preferentially pushed to grain/cell boundaries in LPBF aluminum alloy [23,75]. So far, a couple of particle pushing/engulfment models have been proposed, predicting that a quite high SFV is required (0.1~1 m/s) for capturing a nanoparticle with a radius of less than 100 nm [76]. During LPBF, the SFV (V) is expressed as $V = V_s\cos(\theta)$, related to the laser scanning velocity (V_s) and the angle

between the solidification front normal and the laser scanning direction (θ). From the FE simulation results in Fig. 6(d), the SFV varies from 1.2 m/s to 0.5 m/s with the increase of the melt pool in depth. The SFV at the mid-depth position (at a depth of ~15 μm) is estimated as 0.93 m/s. As a reference, the motion of the solidification front (melt pool rear wall) at the mid-depth position of the melt pool was monitored in-situ by high-speed synchrotron X-ray imaging on an aluminum alloy, as shown in Fig. 5(b1) with an identical laser scanning speed to the studied TiB_2/Al composite (1200 mm/s). The measured SFV is fluctuated in the range of 0.2~1 m/s from the results in Fig. 5(b2). Despite of their differences, both simulated and in-situ observed melt pools indicate a rather high SFV with a magnitude of 10^{-1}~1 m/s at different depth of the melt pool, which enabled the engulfment of nano-TiB_2 particles, as illustrated schematically in Fig. 5 (c3) and (c4). Under the traditional casting condition, a large portion of TiB_2 particles (70 %) that are engulfed in aluminum grains maintain one of two well-defined orientation relationships with the aluminum matrix, i.e. OR1 or OR2 in the current study, tending to form low-energy crystallographic relationships with the matrix in favor of the engulfment [59]. Comparatively, from Figs. 4(d~g) of this study, except for OR1 or OR2, two different ORs (OR3 and OR4) between the engulfed nano-TiB_2 and aluminum matrix are also revealed, indicating the formation of incoherent and high-energy nano-TiB_2/Al interfaces at a high SFV during LPBF.

While the TiB_2 particles and the matrix aluminum grains are refined, a remarkable refinement of intermetallics is also realized by LPBF, appearing as the ubiquitous distribution of the intermetallic nanoparticles throughout the aluminum grains, as

shown in Fig. 3(b). Despite of this, only very limited amount of intragranular intermetallics particles can be observed in LPBF Al-Cu-(Mg) alloys modified with Ti or TiB_2 nanoparticles [22,30,44]. In comparison, in this study, a high number density of intragranular Cu/Ni-rich intermetallic nanoparticles are formed in the TiB_2/Al-2.4Cu-1.7Mg-1.2Ni composite, equivalent to the substitution of ~1.2 wt. % Cu by Ni of the Al2024 alloy. From the simulation in Fig. 5(d), two eutectic reactions are suggested during the solidification of the matrix alloy: L→fcc-Al + Al_3Ni at 617 °C and L→fcc-Al + S (Al_2CuMg) at 515 °C, which is the solidus temperature (T_s). Based on the simulation and the observation of the intermetallics in Figs. 3(b) and 4(a), it is indicative that the intragranular Cu/Ni-rich intermetallic particles precipitated from the liquid as primary solidification phase during the rapid solidification of the melt pool, located inside the aluminum grains. Cu, Mg and the remaining Ni solutes segregated at grain boundaries forming intergranular intermetallics before the completion of the solidification. In addition, a high SFV also results in solute trapping during rapid solidification [77], especially for Cu and Mg in the aluminum matrix (Table S4) and confirmed by the EDS elemental mappings in Fig. 3(c). The evolution of the intermetallics during the solidification of the LPBF composite is summarized in Figs. 5(e) and (f) schematically.

The intermetallic nanoparticles in LPBF TiB_2/Al composite exhibit an ultrafine size of ~70 nm in average, attributed to a rather short diffusion distance for solute elements due to rapid solidification. According to the calculation of an Al-7Si alloy melt, the predicted length of diffusion of solute Si is less than 50 nm at a SFV higher

than 0.05 m/s [78]. In this study, the diffusion coefficients of Cu (4.5×10^{-9} m^2/s) and Ni (3.1×10^{-9} m^2/s) solutes are both at the same magnitude of Si (2.6×10^{-9} m^2/s) at T_l (641 °C) [32]. Consequently, the expected diffusion length of Cu and Ni solutes are the same order of magnitude as the solute diffusion length (several tens of nanometers) at a high SFV, which is close to the size of the Cu/Ni-rich intermetallic nanoparticles in this study. In addition, the Cu/Ni-rich intermetallics are also highly resistant to coarsening under elevated temperatures, indicating that they can maintain the ultrafine size under the periodical thermal influence during LPBF, owing to the low diffusivity and solid solubility of Ni in fcc-Al [33]. A recent work reported the formation of nano-sized thermal stable Al_3Ni intermetallic particles with an ultrafine size of 33 nm dispersed ubiquitously in a LPBF Al-Ni alloy [31], similar to the findings in this study.

Another interesting microstructural feature is the ultrafine nano-cellular networks in the aluminum grains, as presented in Fig. 4(c). As mentioned above, a large fraction of Cu and Mg solutes are trapped by the high SFV during LPBF. The transition of crystal growth modes during solidification has been observed in the sequence of planar → cellular → dendritic → cellular → planar with the increase of SFV [79]. Given a condition of high SFV, a single-phase planar growth is expected above a critical SFV, slightly below which a coupled two-phase growth occurs, forming ultrafine-sized cellular structure, as reported in an Al-4Cu alloy at a critical velocity of 1.7 m/s [77]. Such cellular→planar transition is also indicated in the electrospark deposition of a ternary Al-Li-Cu alloy [80,81]. An ultrafine nano-cellular structure was observed at a high SFV of 1~2 m/s with a cell spacing of ~ 40 nm. The cell boundaries are enriched

in Li/Cu resulted from the entrapment of the Cu and Li solutes. Similarly, in this study, the formation of the intragranular ultrafine nano-cellular structure is attributed to a high SFV of 0.5~1.2 m/s in the melt pool, from the simulation results in Fig. 6(d). The cell boundary is defined by the Cu/Mg-rich network, originated from the entrapment of Cu and Mg solutes. The cell spacing and the solidification conditions can be quantitatively correlated by the Kurz–Giovanola–Trivedi (KGT) model [82,83] (see Supplementary Material C). In this work, given ranges of the simulated SFV (0.5~1.2 m/s) and thermal gradient G (1.3~1.5×10^7 K/m) in Fig. 6(d), the cell spacing is estimated as 26~34 nm, which is close to the observed cell size (~30 nm) in the microstructure of Fig. 4(c).

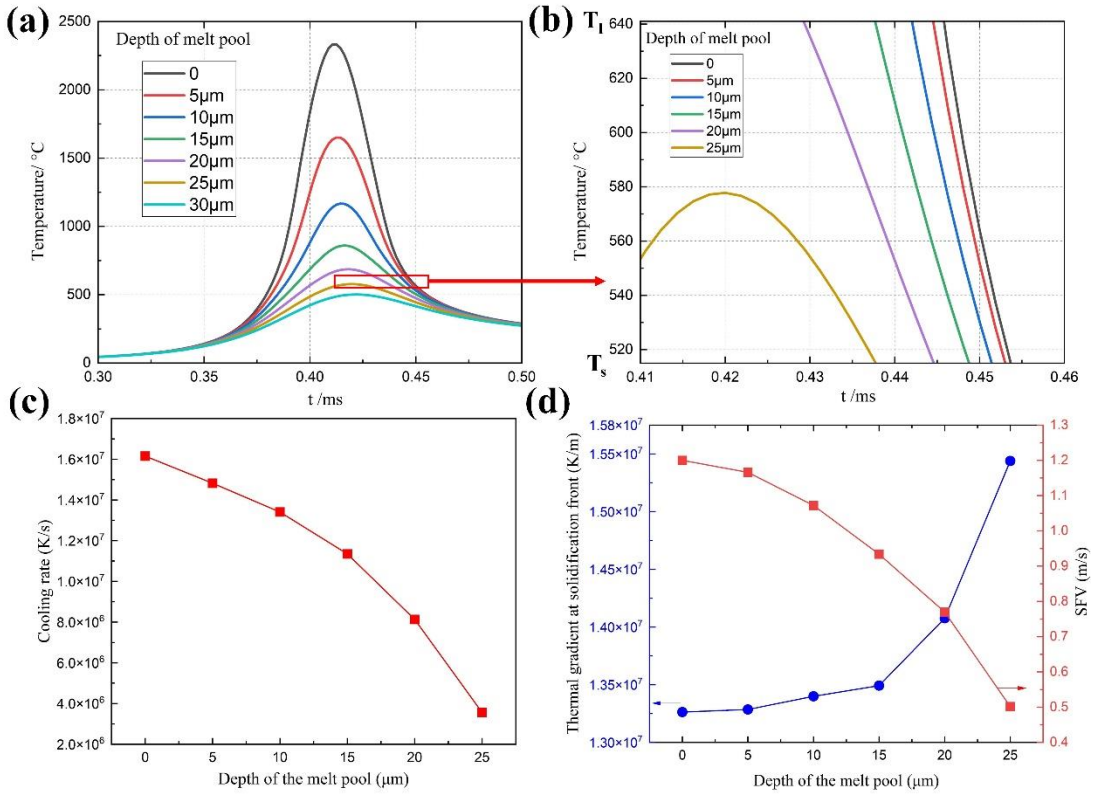

Fig. 6. Simulation results showing (a) temperature variation with time at different positions of the melt pool with (b) the local magnified zone within the solidification temperature range (T_l ~ T_s) during the cooling process; (c) The average cooling rate at

different positions of the melt pool within the solidification temperature range; (d) Temperature gradient and solidification front velocity at different positions of the melt pool.

4.2.Mechanical properties

The LPBF TiB_2/Al composite exhibits a high YS of ~370 MPa, a UTS of ~450 MPa, with an appreciable elongation of ~7 % at the as-built state without post heat treatment. The outstanding mechanical properties are attributed to the greatly refined micro-nano architectured microstructure. Apart from the grain size refinement and solid solution strengthening of the matrix, as commonly reported in LPBF aluminum alloys [84], additional strengthening mechanisms such as geometrically necessary dislocations (GNDs) strengthening and Orowan strengthening are affected by the presence of the bimodal TiB_2 particles, the remarkably refined intermetallic nanoparticles and cellular networks in the LPBF composite. A comprehensive analysis of the strengthening mechanisms associated with the microstructural features is given explicitly (see Supplementary Material D). The contributions of different strengthening mechanisms to YS in LPBF and hot-rolled composites are compared in Fig. 7 graphically, showing a satisfactory prediction between the theoretical and the experimental results as shown in Fig. 7(b).

Specifically, for the LPBF composite, a major increment in strength comes from GND strengthening and Orowan strengthening, while, grain refinement, solid solution strengthening and load bearing strengthening mechanisms show minor contributions to

the YS of the LPBF composite in Fig. 7(a). Compared to the hot-rolled composite, the LPBF composite shows an extraordinary improvement of ~170 MPa in YS, among which the total contribution of grain refinement, solid solution strengthening and load bearing strengthening is only ~40 MPa as shown in Fig. 7(a). Comparatively, the large number of nanoparticles in the LPBF composite result in a remarkable increase of the YS by dislocation strengthening. The GNDs and Orowan strengthening from the nanoparticles in the LPBF composite exceed the summation of GNDs strengthening, Orowan strengthening, and work hardening of its hot-rolled counterpart by ~130 MPa to the YS, as shown in Fig. 7(b). The improvement of YS in the LPBF composite is, therefore, mainly attributed to the high number density and ultrafine intragranular TiB_2 and intermetallic nanoparticles formed in LPBF.

AM of aluminum alloys has been acknowledged for being effective in grain refinement and solid solution strengthening by solute trapping due to rapid solidification. However, since the low k_{HP} value (Hall-Patch coefficient) of aluminum alloy [68], the strengthening potency from grain refinement is limited (about several tens of MPa) even though the grain size can be refined to the magnitude of several micrometers. The solid solution strengthening effect can be tailored by adjusting the alloy composition through increasing the weight percentages of solid solution elements, such as Mg and Mn in aluminum alloys [84,85]. Nevertheless, the increase in strength is still limited (about 10~20 $MPa \cdot wt.\%^{-1}$), unless large amount solute elements are introduced [86]. In comparison, nanoparticles show a high potential in strengthening (over 200 MPa) by increasing the dislocation density in the aluminum matrix

significantly, especially when the nanoparticles are distributed inside the grains/cells with a large fraction and ultrafine size, according to related works [13,87] and in this study.

The strengthening mechanism for the cellular structure was reported in LPBF AlSi10Mg alloy [88,89]. It was proposed that stress partitioning between aluminum matrix and Si-rich cell boundaries by forming dislocation "forests" around cellular boundaries, which is different from conventional precipitate/particle strengthening for aluminum alloys. A cellular structured AlSi10Mg shows higher YS than its partial or non-cellular structured counterparts [89]. In comparison, the nano-cellular structure in this study has a much finer cell size (~ 30 nm) than that of the LPBF AlSi10Mg alloy (typically several hundreds of nanometers [88,89]). A different strengthening mechanism is possible, which needs further investigation. The quantitative contribution to YS from the nano-cellular structure has been left undiscussed despite of their potential strengthening effects. It should be also noted that the addition of 0.11 wt. %Sc plays mainly a major role in modifying the bimodal TiB_2 particulates as demonstrated in Section 4.1. As a result, Al_3Sc phase is unlikely to form according to the Al-Sc phase diagram [90]. The strengthening of Al_3Sc precipitates in other studies [85,91] is, therefore, not expected in the LPBF composite. Moreover, the existence of the pores as shown in Fig. 2(d) will undoubtfully affects the strength and ductility of the LPBF composite adversely [92]. As a result, the experimental YS is slightly lower than the theoretically evaluated YS as shown in Fig. 7(b).

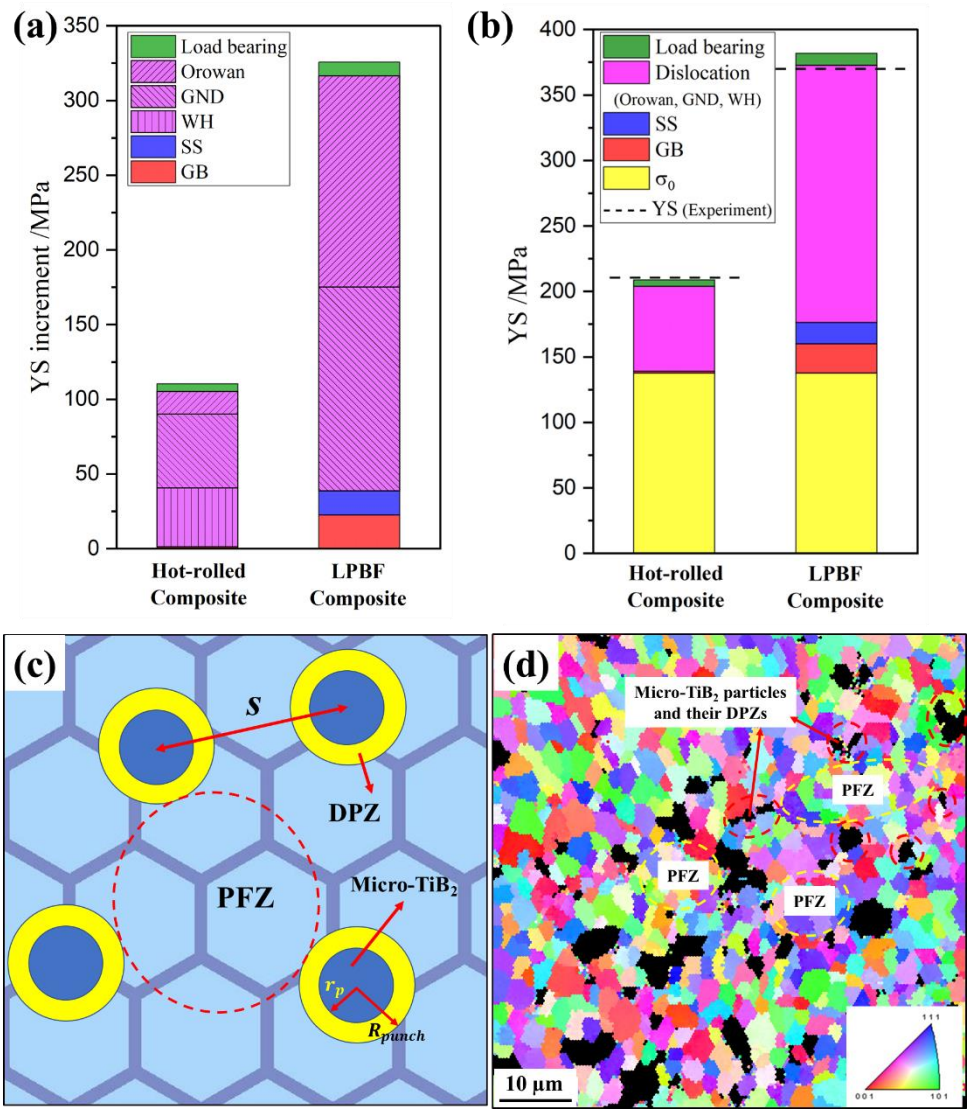

Fig. 7. (a) Stacked histograms showing the YS increment of each known strengthening mechanism individually and (b) Stacked histograms comparing the predicted YS with the experimental YS for the LPBF and hot-rolled composites. (c) Schematic illustration of the DPZ around the reinforcing particles as well as PFZ referring to the LPBF composite with fine grains and uniformly dispersed micro-TiB_2 particles. (d) A local magnified EBSD image showing the DPZ and PFZ in the microstructure.

The LPBF composite also shows a significantly higher ductility than its hot-rolled counterparts and superior to the hot-rolled alloys at both as-rolled and T6 state, as shown in Fig. 1(b). Apparently, the enhanced ductility is attributed to the uniform

distribution of both nano-TiB_2 and refined intermetallic particles in the LPBF samples. It was reported that the spatial arrangement of the particles influences the ductility by affecting the deformation of neighboring grains [93]. According to Ashby's theory [94], when the local stress around the reinforcement exceeds the yield strength of the matrix, the dislocation loops are punched out into the matrix and accumulating inside a "dislocation punched zone" (DPZ) around the particles. The strength is enhanced inside the DPZ due to a localized high density of dislocations. As a result, a DPZ acts as a single hard domain, while the matrix outside the DPZ acts as a soft domain comparatively, called "particle free zone" (PFZ) in referencing to others [87,95]. For the uniformly distributed micro-TiB_2 particulates in the LPBF composites, the size of DPZ ($2R_{\mathrm{punch}}$) is calculated as 1.12 μm from Eqs. S28~S30 (see Supplementary Material D). Given the total micro-TiB_2 volume fraction, the average interparticle spacing (s) of the micro-TiB_2 particulates is estimated as 2.4 μm by Eq. 2, larger than the size of DPZ. In this situation, the DPZ around each particulate is almost isolated, as noted in Fig. 7(c) and evidenced by the EBSD image in Fig. 7(d). It was proposed that the grains in PFZ have higher deformability for strain bearing and retarding the propagation of cracks into the neighboring DPZ zones [87,96]. Meanwhile, shear bands initiated in PFZ can be arrested in DPZ of higher yield strength, suppressing the shear band extension [97]. As a result, the ductility and the strength can be simultaneously increased. In contrast, in the hot-rolled composites, most TiB_2 particulates agglomerate at the grain boundaries as shown in Fig. S1(d), causing the embrittlement of the grain boundaries and limiting the deformation of matrix grains.

Overall, the LPBF composite in this study shows remarkable higher YS and UTS, as well as superior ductility than the hot-rolled alloy and composite at T6 state, attributed to the unique microstructural features generated by LPBF. Further strengthening is potential by aging treatment, as reported for other LPBF Al-Cu-Mg alloys [25,46]. Economically, the LPBF composite is also competitive to other additive manufactured Al-Sc alloys (such as Scalmalloy®) [10,11] due to a much less Sc content. In addition to the outstanding mechanical properties at ambient temperature, the mechanical properties of the LPBF composite at elevated temperatures are also promising. Firstly, the greatly refined microstructure features (grain size, bimodal sized TiB_2 particle, intermetallic phases) can still provide superior strengthening effects at elevated temperature than the traditional casting microstructures. Secondly, the Al-Ni-(Cu) type intermetallics, such as Al_3Ni, τ-Al_7Cu_4Ni, and Al_3(Ni, Cu) are thermally stable and coarsening at a very low rate due to the low diffusion coefficient of Ni in the aluminum matrix at elevated temperature, resulting in exceptional mechanical properties and heat resistance [31,37]. Additionally, the inherent thermal stable TiB_2 ceramic particles generally maintain the particulate strengthening effect at elevated temperatures. The intergranular micro-TiB_2 particulates inhibit the growth of aluminum grains following Zener-pinning mechanism, strengthening the grain boundaries and maintaining a fine grain size [98]. Therefore, the high-strength LPBF composite of this work is a promising candidate for applications as engine components of complex geometry for the automobile and aerospace industries.

5. Conclusions

A TiB_2/Al-Cu-Mg-Ni composite is additive manufactured by LPBF of gas-atomized composite powders containing in-situ TiB_2 particulates in the presence of a minor amount of Sc. The composite almost doubles the strength of its wrought matrix alloy, being one of the best among LPBF Al-Cu-Mg alloys and their composites, associated with its unique highly refined micro-nano hierarchical microstructure. The following conclusions are drawn.

In the LPBF composite, micro-sized TiB_2 particulates are dispersed uniformly inside a refined aluminum matrix of an average grain size of ~3 μm. Meanwhile, nano-sized TiB_2 and Cu/Ni-rich intermetallic particles are dispersed ubiquitously throughout of the aluminum grains. The TiB_2 nanoparticles are formed from the partial dissolution of the micro-TiB_2 particulates and the enrichment of Sc during LPBF. Meanwhile the formation of intermetallic nanoparticles is attributed to the high cooling rate of the melt pool in solidification. Additionally, ultrafine nano-cellular networks (cell size 30 nm) defined by Cu/Mg-rich cell walls formed inside the equiaxed aluminum grains.

The LPBF composite presents superior mechanical properties with a yield strength of ~370 MPa, an ultimate tensile strength of ~450 MPa and an elongation of ~7 %. Quantitative analyses reveal the major strengthening mechanisms being GNDs and Orowan dislocation strengthening, a synergistic effect of the bimodal TiB_2 particles and intermetallic nanoparticles, and potentially the nano-cellular networks inside the aluminum grains. The ductility is improved simultaneously by the uniform spatial arrangement of the bimodal particulates.

The main contributions and novelty of the research are given in the following.

LPBF greatly refines the microstructure of TiB_2/Al-Cu-Mg-Ni composite, resulting in ubiquitous bimodal TiB_2 reinforcing particles in the alloy matrix. Meanwhile, intermetallics are refined as ultrafine nanoparticles. Additionally, the formation of nano-cellular network that have rarely been reported in LPBF Al alloys and composites is revealed. These shed light on the role of additive manufacturing in tailoring the microstructure of particulate reinforced MMCs.

The LPBF TiB_2/Al composite show mechanical properties comparable to the T6 commercial wrought Al2618 alloy and composites and being one of the best among LPBF Al-Cu-Mg alloys and their composites. The novel LPBF TiB_2/Al composite is a promising candidate lightweight high-strength material for additive manufacturing components of complex geometry for automobile and aerospace industries.

Acknowledgement

The authors acknowledge Chven Mitchell who assisted/acquired the image of Figs. 2(d) and 2(e) for this paper on a Zeiss Xradia 510 Versa 3D X-ray Microscope that was supported by the EVPRP Major Multi-User Equipment Program 2017 at Purdue University. SM acknowledges the Graduate School of Purdue University for granting a Ross Fellowship and a Bilsland Dissertation Fellowship for his graduate study. XW acknowledges the Purdue Research Foundation for a Trask Award for the work.

References

[1] T.D. Ngo, A. Kashani, G. Imbalzano, K.T.Q. Nguyen, D. Hui, Additive manufacturing (3D printing): A review of materials, methods, applications and challenges, Compos. Part B Eng. 143 (2018) 172–196. https://doi.org/10.1016/j.compositesb.2018.02.012.

[2] J.H. Martin, B.D. Yahata, J.M. Hundley, J.A. Mayer, T.A. Schaedler, T.M. Pollock, 3D printing of high-strength aluminium alloys, Nature. 549 (2017) 365–369. https://doi.org/10.1038/nature23894.

[3] D. Gu, X. Shi, R. Poprawe, D.L. Bourell, R. Setchi, J. Zhu, Material-structure-performance integrated laser-metal additive manufacturing, Science (80-.). 372 (2021). https://doi.org/10.1126/science.abg1487.

[4] N.T. Aboulkhair, M. Simonelli, L. Parry, I. Ashcroft, C. Tuck, R. Hague, 3D printing of Aluminium alloys: Additive Manufacturing of Aluminium alloys using selective laser melting, Prog. Mater. Sci. 106 (2019) 100578. https://doi.org/10.1016/j.pmatsci.2019.100578.

[5] W.H. Yu, S.L. Sing, C.K. Chua, C.N. Kuo, X.L. Tian, Particle-reinforced metal matrix nanocomposites fabricated by selective laser melting: A state of the art review, Prog. Mater. Sci. 104 (2019) 330–379. https://doi.org/10.1016/j.pmatsci.2019.04.006.

[6] L. Thijs, K. Kempen, J.P. Kruth, J. Van Humbeeck, Fine-structured aluminium products with controllable texture by selective laser melting of pre-alloyed AlSi10Mg powder, Acta Mater. 61 (2013) 1809–1819. https://doi.org/10.1016/j.actamat.2012.11.052.

[7] X. Liu, Y. Liu, Z. Zhou, K. Wang, Q. Zhan, X. Xiao, Grain refinement and crack inhibition of selective laser melted AA2024 aluminum alloy via inoculation with $TiC–TiH_2$, Mater. Sci. Eng. A. 813 (2021) 141171. https://doi.org/10.1016/j.msea.2021.141171.

[8] A.B. Spierings, K. Dawson, T. Heeling, P.J. Uggowitzer, R. Schäublin, F. Palm, K. Wegener, Microstructural features of Sc- and Zr-modified Al-Mg

alloys processed by selective laser melting, Mater. Des. 115 (2017) 52–63. https://doi.org/10.1016/j.matdes.2016.11.040.

[9] Z. Wang, X. Lin, N. Kang, Y. Hu, J. Chen, W. Huang, Strength-ductility synergy of selective laser melted Al-Mg-Sc-Zr alloy with a heterogeneous grain structure, Addit. Manuf. 34 (2020) 101260. https://doi.org/10.1016/j.addma.2020.101260.

[10] K. Schmidtke, F. Palm, A. Hawkins, C. Emmelmann, Process and mechanical properties: Applicability of a scandium modified Al-alloy for laser additive manufacturing, Phys. Procedia. 12 (2011) 369–374. https://doi.org/10.1016/j.phpro.2011.03.047.

[11] A.B. Spierings, K. Dawson, K. Kern, F. Palm, K. Wegener, SLM-processed Sc- and Zr- modified Al-Mg alloy: Mechanical properties and microstructural effects of heat treatment, Mater. Sci. Eng. A. 701 (2017) 264–273. https://doi.org/10.1016/j.msea.2017.06.089.

[12] Z. Zhu, F.L. Ng, H.L. Seet, W. Lu, C.H. Liebscher, Z. Rao, D. Raabe, S. Mui Ling Nai, Superior mechanical properties of a selective-laser-melted AlZnMgCuScZr alloy enabled by a tunable hierarchical microstructure and dual-nanoprecipitation, Mater. Today. 52 (2022) 90–101. https://doi.org/10.1016/j.mattod.2021.11.019.

[13] T.C. Lin, C. Cao, M. Sokoluk, L. Jiang, X. Wang, J.M. Schoenung, E.J. Lavernia, X. Li, Aluminum with dispersed nanoparticles by laser additive manufacturing, Nat. Commun. 10 (2019) 1–9. https://doi.org/10.1038/s41467-019-12047-2.

[14] M.N. Patel, D. Qiu, G. Wang, M.A. Gibson, A. Prasad, D.H. StJohn, M.A. Easton, Understanding the refinement of grains in laser surface remelted Al–Cu alloys, Scr. Mater. 178 (2020) 447–451. https://doi.org/10.1016/j.scriptamat.2019.12.020.

[15] A. Prasad, L. Yuan, P. Lee, M. Patel, D. Qiu, M. Easton, D. StJohn, Towards understanding grain nucleation under Additive Manufacturing solidification conditions, Acta Mater. 195 (2020) 392–403.

https://doi.org/10.1016/j.actamat.2020.05.012.

[16] D.D. Gu, W. Meiners, K. Wissenbach, R. Poprawe, Laser additive manufacturing of metallic components: Materials, processes and mechanisms, Int. Mater. Rev. 57 (2012) 133–164. https://doi.org/10.1179/1743280411Y.0000000014.

[17] B. Li, B. Qian, Y. Xu, Z. Liu, J. Zhang, F. Xuan, Additive manufacturing of ultrafine-grained austenitic stainless steel matrix composite via vanadium carbide reinforcement addition and selective laser melting: Formation mechanism and strengthening effect, Mater. Sci. Eng. A. 745 (2019) 495–508. https://doi.org/10.1016/j.msea.2019.01.008.

[18] W. Li, Y. Yang, J. Liu, Y. Zhou, M. Li, S. Wen, Q. Wei, C. Yan, Y. Shi, Enhanced nanohardness and new insights into texture evolution and phase transformation of TiAl/TiB_2 in-situ metal matrix composites prepared via selective laser melting, Acta Mater. 136 (2017) 90–104. https://doi.org/10.1016/j.actamat.2017.07.003.

[19] S.C. Tjong, K.C. Lau, Properties and abrasive wear of TiB_2/Al-4%Cu composites produced by hot isostatic pressing, Compos. Sci. Technol. 59 (1999) 2005–2013. https://doi.org/10.1016/S0266-3538(99)00056-1.

[20] X. Wang, Z. Liu, W. Dai, Q. Han, On the Understanding of Aluminum Grain Refinement by Al-Ti-B Type Master Alloys, Metall. Mater. Trans. B Process Metall. Mater. Process. Sci. 46 (2015) 1620–1625. https://doi.org/10.1007/s11663-014-0252-3.

[21] Y. Tang, Z. Chen, A. Borbély, G. Ji, S.Y. Zhong, D. Schryvers, V. Ji, H.W. Wang, Quantitative study of particle size distribution in an in-situ grown Al-TiB2 composite by synchrotron X-ray diffraction and electron microscopy, Mater. Charact. 102 (2015) 131–136. https://doi.org/10.1016/j.matchar.2015.03.003.

[22] P. Mair, L. Kaserer, J. Braun, N. Weinberger, I. Letofsky-Papst, G. Leichtfried, Microstructure and mechanical properties of a TiB_2-modified Al–Cu alloy processed by laser powder-bed fusion, Mater. Sci. Eng. A. 799 (2021) 140209.

https://doi.org/10.1016/j.msea.2020.140209.

[23] X.P. Li, G. Ji, Z. Chen, A. Addad, Y. Wu, H.W. Wang, J. Vleugels, J. Van Humbeeck, J.P. Kruth, Selective laser melting of nano-TiB_2 decorated AlSi10Mg alloy with high fracture strength and ductility, Acta Mater. 129 (2017) 183–193. https://doi.org/10.1016/j.actamat.2017.02.062.

[24] X. Wen, Q. Wang, Q. Mu, N. Kang, S. Sui, H. Yang, X. Lin, W. Huang, Laser solid forming additive manufacturing TiB_2 reinforced 2024Al composite: Microstructure and mechanical properties, Mater. Sci. Eng. A. 745 (2019) 319–325. https://doi.org/10.1016/j.msea.2018.12.072.

[25] P. Wang, C. Gammer, F. Brenne, T. Niendorf, J. Eckert, S. Scudino, A heat treatable TiB_2/Al-3.5Cu-1.5Mg-1Si composite fabricated by selective laser melting: Microstructure, heat treatment and mechanical properties, Compos. Part B Eng. 147 (2018) 162–168. https://doi.org/10.1016/j.compositesb.2018.04.026.

[26] J. Sun, X. Wang, L. Guo, X. Zhang, H. Wang, Synthesis of nanoscale spherical TiB_2 particles in Al matrix by regulating Sc contents, J. Mater. Res. 34 (2019) 1258–1265. https://doi.org/10.1557/jmr.2018.469.

[27] Q. Wang, Y. Li, S. Chen, X. Liu, Z. Chen, M. Wang, H. Zhu, H. Wang, Interface alloying design to improve the dispersion of TiB_2 nanoparticles in Al composites: A first-principles study, J. Phys. Chem. C. 125 (2021) 5937–5946. https://doi.org/10.1021/acs.jpcc.1c00371.

[28] Y. Du, X. You, F. Qiao, L. Guo, Z. Liu, A model for predicting the temperature field during selective laser melting, Results Phys. 12 (2019) 52–60. https://doi.org/10.1016/j.rinp.2018.11.031.

[29] F. Leijon, E. Johansson, J. Lu, B. Aling, S. Skjervold, J. Moverare, Investigation of Ti1−x(Zr,Ta,V,W)xB_2 and Al3Ti1−x(Zr,V)x grain refiners in additively manufactured Al-2 wt%Cu alloys by a high throughput method, Mater. Des. 222 (2022) 111093. https://doi.org/10.1016/j.matdes.2022.111093.

[30] C.A. Biffi, P. Bassani, J. Fiocchi, M. Albu, A. Tuissi, Selective laser melting of AlCu-TiB_2 alloy using pulsed wave laser emission mode: processability,

microstructure and mechanical properties, Mater. Des. 204 (2021). https://doi.org/10.1016/j.matdes.2021.109628.

[31] J. Deng, C. Chen, X. Liu, Y. Li, K. Zhou, S. Guo, A high-strength heat-resistant Al−5.7Ni eutectic alloy with spherical Al_3Ni nano-particles by selective laser melting, Scr. Mater. 203 (2021) 114034. https://doi.org/10.1016/j.scriptamat.2021.114034.

[32] Y. Du, Y.A. Chang, B. Huang, W. Gong, Z. Jin, H. Xu, Z. Yuan, Y. Liu, Y. He, F.Y. Xie, Diffusion coefficients of some solutes in fcc and liquid Al: Critical evaluation and correlation, Mater. Sci. Eng. A. 363 (2003) 140–151. https://doi.org/10.1016/S0921-5093(03)00624-5.

[33] R.A. Michi, A. Plotkowski, A. Shyam, R.R. Dehoff, S.S. Babu, Towards high-temperature applications of aluminium alloys enabled by additive manufacturing, Int. Mater. Rev. 67 (2022) 298–345. https://doi.org/10.1080/09506608.2021.1951580.

[34] K.C. Chang, J.R. Zhao, F.Y. Hung, Effects of hyper-high-temperature solid-solution treatment on microstructure evolution and nanoprecipitation of the Al-Ni-Cu-Fe-Zr-Sc alloy manufactured by selective laser melting, J. Alloys Compd. 883 (2021) 160781. https://doi.org/10.1016/j.jallcom.2021.160781.

[35] D.R. Manca, A.Y. Churyumov, A. V. Pozdniakov, D.K. Ryabov, V.A. Korolev, D.K. Daubarayte, Novel heat-resistant Al-Si-Ni-Fe alloy manufactured by selective laser melting, Mater. Lett. 236 (2019) 676–679. https://doi.org/10.1016/j.matlet.2018.11.033.

[36] J.T. Kim, V. Soprunyuk, N. Chawake, Y.H. Zheng, F. Spieckermann, S.H. Hong, K.B. Kim, J. Eckert, Outstanding strengthening behavior and dynamic mechanical properties of in-situ Al–Al3Ni composites by Cu addition, Compos. Part B Eng. 189 (2020) 107891. https://doi.org/10.1016/j.compositesb.2020.107891.

[37] E.M. Elgallad, P. Shen, Z. Zhang, X. Chen, Effects of heat treatment on the microstructure and mechanical properties of AA2618 DC cast alloy, Mater. Des. 61 (2014) 133–140. https://doi.org/10.1016/j.matdes.2014.04.045.

[38] L. Ceschini, A. Morri, A. Morri, M. Di Sabatino, Effect of thermal exposure on the residual hardness and tensile properties of the EN AW-2618A piston alloy, Mater. Sci. Eng. A. 639 (2015) 288–297. https://doi.org/10.1016/j.msea.2015.04.080.

[39] S. Ma, Y. Wang, X. Wang, Microstructures and mechanical properties of an Al-Cu-Mg-Sc alloy reinforced with in-situ TiB2 particulates, Mater. Sci. Eng. A. Struct. Mater. 788 (2020) 139603. https://doi.org/10.1016/j.msea.2020.139603.

[40] S. Ma, X. Wang, The effects of hot rolling and heat treatment on the microstructure and mechanical properties of an Al-Cu-Mg-Sc alloy reinforced with in situ TiB_2 particulates, J. Mater. Res. 37 (2022) 3680–3694. https://doi.org/10.1557/s43578-022-00741-9.

[41] M. Klinger, More features, more tools, more CrysTBox, J. Appl. Crystallogr. 50 (2017) 1226–1234.

[42] Y. Huang, T.G. Fleming, S.J. Clark, S. Marussi, K. Fezzaa, J. Thiyagalingam, C.L.A. Leung, P.D. Lee, Keyhole fluctuation and pore formation mechanisms during laser powder bed fusion additive manufacturing, Nat. Commun. 13 (2022) 1–11. https://doi.org/10.1038/s41467-022-28694-x.

[43] Q.Z. Wang, X. Lin, N. Kang, X.L. Wen, Y. Cao, J.L. Lu, D.J. Peng, J. Bai, Y.X. Zhou, M. El Mansori, W.D. Huang, Effect of laser additive manufacturing on the microstructure and mechanical properties of TiB_2 reinforced Al-Cu matrix composite, Mater. Sci. Eng. A. 840 (2022). https://doi.org/10.1016/j.msea.2022.142950.

[44] Q. Tan, J. Zhang, Q. Sun, Z. Fan, G. Li, Y. Yin, Y. Liu, M.X. Zhang, Inoculation treatment of an additively manufactured 2024 aluminium alloy with titanium nanoparticles, Acta Mater. 196 (2020) 1–16. https://doi.org/10.1016/j.actamat.2020.06.026.

[45] L. Pantělejev, D. Koutný, D. Paloušek, J. Kaiser, Mechanical and microstructural properties of 2618 Al-Alloy processed by SLM remelting strategy, Mater. Sci. Forum. 891 MSF (2017) 343–349.

https://doi.org/10.4028/www.scientific.net/MSF.891.343.

[46] F. Belelli, R. Casati, F. Larini, M. Riccio, M. Vedani, Investigation on two Ti–B-reinforced Al alloys for Laser Powder Bed Fusion, Mater. Sci. Eng. A. 808 (2021) 140944. https://doi.org/10.1016/j.msea.2021.140944.

[47] F. Belelli, R. Casati, M. Riccio, A. Rizzi, M.Y. Kayacan, M. Vedani, Development of a Novel High-Temperature Al Alloy for Laser Powder Bed Fusion, Met. . 11 (2021). https://doi.org/10.3390/met11010035.

[48] M.H. Ghoncheh, M. Sanjari, A.S. Zoeram, E. Cyr, B.S. Amirkhiz, A. Lloyd, M. Haghshenas, M. Mohammadi, On the microstructure and solidification behavior of new generation additively manufactured Al-Cu-Mg-Ag-Ti-B alloys, Addit. Manuf. 37 (2021) 101724. https://doi.org/10.1016/j.addma.2020.101724.

[49] M. Avateffazeli, P.E. Carrion, B. Shachi-Amirkhiz, H. Pirgazi, M. Mohammadi, N. Shamsaei, M. Haghshenas, Correlation between tensile properties, microstructure, and processing routes of an Al–Cu–Mg–Ag–TiB_2 (A205) alloy: Additive manufacturing and casting, Mater. Sci. Eng. A. 841 (2022) 142989. https://doi.org/10.1016/j.msea.2022.142989.

[50] M. Tan, Q. Xin, Z. Li, B.Y. Zong, Influence of SiC and Al_2O_3 particulate reinforcements and heat treatments on mechanical properties and damage evolution of Al-2618 metal matrix composites, J. Mater. Sci. 36 (2001) 2045–2053. https://doi.org/10.1023/A:1017591117670.

[51] K. Yu, W. Li, S. Li, J. Zhao, Mechanical properties and microstructure of aluminum alloy 2618 with Al3(Sc. Zr) phases, Mater. Sci. Eng. A. 368 (2004) 88–93. https://doi.org/10.1016/j.msea.2003.09.092.

[52] A. Sakthivel, R. Palaninathan, R. Velmurugan, P. Raghothama Rao, Production and mechanical properties of SiCp particle-reinforced 2618 aluminum alloy composites, J. Mater. Sci. 43 (2008) 7047–7056. https://doi.org/10.1007/s10853-008-3033-z.

[53] J. Wang, D. Yi, X. Su, F. Yin, Influence of deformation ageing treatment on microstructure and properties of aluminum alloy 2618, Mater. Charact. 59

(2008) 965–968. https://doi.org/10.1016/j.matchar.2007.08.007.

[54] R. Casati, J. Fiocchi, A. Fabrizi, N. Lecis, F. Bonollo, M. Vedani, Effect of ball milling on the ageing response of Al2618 composites reinforced with SiC and oxide nanoparticles, J. Alloys Compd. 693 (2017) 909–920. https://doi.org/10.1016/j.jallcom.2016.09.265.

[55] H.W. Liu, F. Wang, B.Q. Xiong, Y.A. Zhang, Z.H. Li, X.W. Li, S.H. Huang, Microstructure and mechanical properties of an Al-Cu-Mg-Fe-Ni alloy, Adv. Mater. Res. 988 (2014) 156–160. https://doi.org/10.4028/www.scientific.net/AMR.988.156.

[56] Q. Tan, J. Zhang, N. Mo, Z. Fan, Y. Yin, M. Bermingham, Y. Liu, H. Huang, M.X. Zhang, A novel method to 3D-print fine-grained AlSi10Mg alloy with isotropic properties via inoculation with LaB_6 nanoparticles, Addit. Manuf. 32 (2020) 101034. https://doi.org/10.1016/j.addma.2019.101034.

[57] J. Huang, L. Feng, C. Li, C. Huang, J. Li, B. Friedrich, Mechanism of Sc poisoning of Al-5Ti-1B grain refiner, Scr. Mater. 180 (2020) 88–92. https://doi.org/10.1016/j.scriptamat.2020.01.031.

[58] Y. Ma, A. Addad, G. Ji, M.X. Zhang, W. Lefebvre, Z. Chen, V. Ji, Atomic-scale investigation of the interface precipitation in a TiB_2 nanoparticles reinforced Al–Zn–Mg–Cu matrix composite, Acta Mater. 185 (2020) 287–299. https://doi.org/10.1016/j.actamat.2019.11.068.

[59] P.L. Schaffer, D.N. Miller, A.K. Dahle, Crystallography of engulfed and pushed TiB_2 particles in aluminium, Scr. Mater. 57 (2007) 1129–1132. https://doi.org/10.1016/j.scriptamat.2007.08.009.

[60] C.L.A. Leung, S. Marussi, M. Towrie, R.C. Atwood, P.J. Withers, P.D. Lee, The effect of powder oxidation on defect formation in laser additive manufacturing, Acta Mater. 166 (2019) 294–305. https://doi.org/10.1016/j.actamat.2018.12.027.

[61] H. Li, Y. Huang, S. Jiang, Y. Lu, X. Gao, X. Lu, Z. Ning, J. Sun, Columnar to equiaxed transition in additively manufactured CoCrFeMnNi high entropy alloy, Mater. Des. 197 (2021). https://doi.org/10.1016/j.matdes.2020.109262.

[62] N.J. Finch, Mutual Solubilities of Titanium and Boron in Pure Aluminum., Met. Trans. 3 (1972) 2709–2711. https://doi.org/10.1007/BF02644250.

[63] B. Jiang, L. Zhenglong, C. Xi, L. Peng, L. Nannan, C. Yanbin, Microstructure and mechanical properties of TiB_2-reinforced 7075 aluminum matrix composites fabricated by laser melting deposition, Ceram. Int. 45 (2019) 5680–5692. https://doi.org/10.1016/j.ceramint.2018.12.033.

[64] S.J. Clark, C.L.A. Leung, Y. Chen, L. Sinclair, S. Marussi, P.D. Lee, Capturing Marangoni flow via synchrotron imaging of selective laser melting, IOP Conf. Ser. Mater. Sci. Eng. 861 (2020). https://doi.org/10.1088/1757-899X/861/1/012010.

[65] J.H. Martin, B. Yahata, J. Mayer, R. Mone, E. Stonkevitch, J. Miller, M.R. O'Masta, T. Schaedler, J. Hundley, P. Callahan, T. Pollock, Grain refinement mechanisms in additively manufactured nano-functionalized aluminum, Acta Mater. 200 (2020) 1022–1037. https://doi.org/10.1016/j.actamat.2020.09.043.

[66] Y. Chen, S.J. Clark, D.M. Collins, S. Marussi, S.A. Hunt, D.M. Fenech, T. Connolley, R.C. Atwood, O. V. Magdysyuk, G.J. Baxter, M.A. Jones, C.L.A. Leung, P.D. Lee, Correlative Synchrotron X-ray Imaging and Diffraction of Directed Energy Deposition Additive Manufacturing, Acta Mater. 209 (2021) 116777. https://doi.org/10.1016/j.actamat.2021.116777.

[67] D. Gu, H. Wang, D. Dai, P. Yuan, W. Meiners, R. Poprawe, Rapid fabrication of Al-based bulk-form nanocomposites with novel reinforcement and enhanced performance by selective laser melting, Scr. Mater. 96 (2015) 25–28. https://doi.org/10.1016/j.scriptamat.2014.10.011.

[68] M. Wang, D. Chen, Z. Chen, Y. Wu, F. Wang, N. Ma, H. Wang, Mechanical properties of in-situ TiB_2/A356 composites, Mater. Sci. Eng. A. 590 (2014) 246–254. https://doi.org/10.1016/j.msea.2013.10.021.

[69] M.E. Hyman, C. McCullough, C.G. Levi, R. Mehrabian, Evolution of boride morphologies in TiAl-B alloys, Metall. Trans. A. 22 (1991) 1647–1662. https://doi.org/10.1007/BF02667377.

[70] M.E. Van Dalen, D.C. Dunand, D.N. Seidman, Effects of Ti additions on the

nanostructure and creep properties of precipitation-strengthened Al-Sc alloys, Acta Mater. 53 (2005) 4225–4235. https://doi.org/10.1016/j.actamat.2005.05.022.

[71] N.L. Yue, L. Lu, M.O. Lai, Application of thermodynamic calculation in the in-situ process of Al/TiB_2, Compos. Struct. 47 (1999) 691–694. https://doi.org/https://doi.org/10.1016/S0263-8223(00)00037-4.

[72] A.L. Greer, A.M. Bunn, A. Tronche, P. V Evans, D.J. Bristow, Modelling of inoculation of metallic melts: application to grain refinement of aluminium by Al–Ti–B, Acta Mater. 48 (2000) 2823–2835. https://doi.org/10.1016/S1359-6454(00)00094-X.

[73] D.H. Stjohn, M. Qian, M.A. Easton, P. Cao, The Interdependence Theory: The relationship between grain formation and nucleant selection, Acta Mater. 59 (2011) 4907–4921. https://doi.org/10.1016/j.actamat.2011.04.035.

[74] B.Q. Han, D.C. Dunand, Microstructure and mechanical properties of magnesium containing high volume fractions of yttria dispersoids, Mater. Sci. Eng. A. 277 (2000) 297–304. https://doi.org/10.1016/S0921-5093(99)00074-X.

[75] Q. Yang, Y. Ma, Z. Chen, G. Ji, M.L. Wang, S.Y. Zhong, Y. Wu, V. Ji, H.W. Wang, A new powder metallurgy routine to fabricate TiB_2/Al–Zn–Mg–Cu nanocomposites based on composite powders with pre-embedded nanoparticles, Materialia. 8 (2019). https://doi.org/10.1016/j.mtla.2019.100458.

[76] D. Shangguan, S. Ahuja, D.M. Stefanescu, An analytical model for the interaction between an insoluble particle and an advancing solid/liquid interface, Metall. Trans. A. 23 (1992) 669–680. https://doi.org/10.1007/BF02801184.

[77] V. Bathula, C. Liu, K. Zweiacker, J. McKeown, J.M.K. Wiezorek, Interface velocity dependent solute trapping and phase selection during rapid solidification of laser melted hypo-eutectic Al-11at.%Cu alloy, Acta Mater. 195 (2020) 341–357. https://doi.org/10.1016/j.actamat.2020.04.006.

[78] J.K. Kim, P.K. Rohatgi, The effect of the diffusion of solute between the particle and the interface on the particle pushing phenomena, Acta Mater. 46

(1998) 1115–1123. https://doi.org/10.1016/S1359-6454(97)00331-5.

[79] W. Kurz, R. Trivedi, Rapid solidification processing and microstructure formation, Mater. Sci. Eng. A. 179–180 (1994) 46–51. https://doi.org/10.1016/0921-5093(94)90162-7.

[80] D.W. Heard, R. Gauvin, M. Brochu, Non-equilibrium solute partitioning in a laser re-melted Al-Li-Cu alloy, Acta Mater. 61 (2013) 7432–7436. https://doi.org/10.1016/j.actamat.2013.08.050.

[81] D.W. Heard, J. Boselli, R. Rioja, E.A. Marquis, R. Gauvin, M. Brochu, Interfacial morphology development and solute trapping behavior during rapid solidification of an Al-Li-Cu alloy, Acta Mater. 61 (2013) 1571–1580. https://doi.org/10.1016/j.actamat.2012.11.034.

[82] W. Kurz, B. Giovanola, R. Trivedi, Theory of microstructural development during rapid solidification, Acta Metall. 34 (1986) 823–830. https://doi.org10.1016/0001-6160(86)90056-8.

[83] R. Trivedi, W. Kurz, Dendritic growth, Int. Mater. Rev. 39 (1994) 49–74. https://doi.org/10.1179/imr.1994.39.2.49.

[84] R. Li, M. Wang, Z. Li, P. Cao, T. Yuan, H. Zhu, Developing a high-strength Al-Mg-Si-Sc-Zr alloy for selective laser melting: Crack-inhibiting and multiple strengthening mechanisms, Acta Mater. 193 (2020) 83–98. https://doi.org/10.1016/j.actamat.2020.03.060.

[85] Q. Jia, P. Rometsch, P. Kürnsteiner, Q. Chao, A. Huang, M. Weyland, L. Bourgeois, X. Wu, Selective laser melting of a high strength Al-Mn-Sc alloy: Alloy design and strengthening mechanisms, Acta Mater. 171 (2019) 108–118. https://doi.org/10.1016/j.actamat.2019.04.014.

[86] K. Ma, H. Wen, T. Hu, T.D. Topping, D. Isheim, D.N. Seidman, E.J. Lavernia, J.M. Schoenung, Mechanical behavior and strengthening mechanisms in ultrafine grain precipitation-strengthened aluminum alloy, Acta Mater. 62 (2014) 141–155. https://doi.org/10.1016/j.actamat.2013.09.042.

[87] L. Jiang, H. Yang, J.K. Yee, X. Mo, T. Topping, E.J. Lavernia, J.M. Schoenung, Toughening of aluminum matrix nanocomposites via spatial arrays

of boron carbide spherical nanoparticles, Acta Mater. 103 (2016) 128–140. https://doi.org/10.1016/j.actamat.2015.09.057.

[88] D.K. Kim, W. Woo, J.H. Hwang, K. An, S.H. Choi, Stress partitioning behavior of an AlSi10Mg alloy produced by selective laser melting during tensile deformation using in situ neutron diffraction, J. Alloys Compd. 686 (2016) 281–286. https://doi.org/10.1016/j.jallcom.2016.06.011.

[89] Z. Li, Z. Li, Z. Tan, D.B. Xiong, Q. Guo, Stress relaxation and the cellular structure-dependence of plastic deformation in additively manufactured AlSi10Mg alloys, Int. J. Plast. 127 (2020) 102640. https://doi.org/10.1016/j.ijplas.2019.12.003.

[90] J. Røyset, N. Ryum, Scandium in aluminium alloys, Int. Mater. Rev. 50 (2005) 19–44. https://doi.org/10.1179/174328005X14311.

[91] C.B. Fuller, D.N. Seidman, D.C. Dunand, Mechanical properties of Al(Sc,Zr) alloys at ambient and elevated temperatures, Acta Mater. 51 (2003) 4803–4814. https://doi.org/10.1016/S1359-6454(03)00320-3.

[92] C.M. Laursen, S.A. DeJong, S.M. Dickens, A.N. Exil, D.F. Susan, J.D. Carroll, Relationship between ductility and the porosity of additively manufactured AlSi10Mg, Mater. Sci. Eng. A. 795 (2020) 139922. https://doi.org/10.1016/j.msea.2020.139922.

[93] K. Wang, H.Y. Jiang, Q.D. Wang, B. Ye, W.J. Ding, Nanoparticle-induced nucleation of eutectic silicon in hypoeutectic Al-Si alloy, Mater. Charact. 117 (2016) 41–46. https://doi.org/10.1016/j.matchar.2016.04.016.

[94] M.F. Ashby, The deformation of plastically non-homogeneous materials, Philos. Mag. A J. Theor. Exp. Appl. Phys. 21 (1970) 399–424. https://doi.org/10.1080/14786437008238426.

[95] X. Rong, D. Zhao, C. He, C. Shi, E. Liu, N. Zhao, Revealing the strengthening and toughening mechanisms of Al-CuO composite fabricated via in-situ solid-state reaction, Acta Mater. 204 (2021) 116524. https://doi.org/10.1016/j.actamat.2020.116524.

[96] R.D. Conner, Y. Li, W.D. Nix, W.L. Johnson, Shear band spacing under

bending of Zr-based metallic glass plates, Acta Mater. 52 (2004) 2429–2434. https://doi.org/10.1016/j.actamat.2004.01.034.

[97] D.C. Hofmann, J.-Y. Suh, A. Wiest, G. Duan, M.-L. Lind, M.D. Demetriou, W.L. Johnson, Designing metallic glass matrix composites with high toughness and tensile ductility, Nature. 451 (2008) 1085–1089. https://doi.org/10.1038/nature06598.

[98] C.S. Goh, J. Wei, L.C. Lee, M. Gupta, Properties and deformation behaviour of Mg–Y_2O_3 nanocomposites, Acta Mater. 55 (2007) 5115–5121. https://doi.org/10.1016/j.actamat.2007.05.032.